

See discussions, stats, and author profiles for this publication at: <https://www.researchgate.net/publication/6207066>

# Crystal structure of the RIM1 $\alpha$ C2B domain at 1.7 Å resolution

ARTICLE *in* BIOCHEMISTRY · SEPTEMBER 2007

Impact Factor: 3.02 · DOI: 10.1021/bi700698a · Source: PubMed

CITATIONS

8

READS

33

7 AUTHORS, INCLUDING:



**Han Dai**

GlaxoSmithKline plc.

25 PUBLICATIONS 1,373 CITATIONS

[SEE PROFILE](#)



**Diana R. Tomchick**

University of Texas Southwestern Medical Ce...

98 PUBLICATIONS 6,114 CITATIONS

[SEE PROFILE](#)



**Irina Dulubova**

Reata Pharmaceuticals

44 PUBLICATIONS 3,023 CITATIONS

[SEE PROFILE](#)



**Mischa Machius**

103 PUBLICATIONS 4,457 CITATIONS

[SEE PROFILE](#)

Published in final edited form as:

*Biochemistry*. 2007 August 7; 46(31): 8988–8998. doi:10.1021/bi700698a.

## Crystal Structure of the RIM1 $\alpha$ C<sub>2</sub>B Domain at 1.7 Å Resolution,<sup>†,¶</sup>

Rong Guan<sup>1,2</sup>, Han Dai<sup>1,2</sup>, Diana R. Tomchick<sup>1</sup>, Irina Dulubova<sup>1,2</sup>, Mischa Machius<sup>1</sup>, Thomas C. Südhof<sup>3,4,5</sup>, and Josep Rizo<sup>1,2,\*</sup>

<sup>1</sup> Department of Biochemistry, University of Texas Southwestern Medical Center, 6000 Harry Hines Blvd., Dallas, TX 75390

<sup>2</sup> Department of Pharmacology, University of Texas Southwestern Medical Center, 6000 Harry Hines Blvd., Dallas, TX 75390

<sup>3</sup> Department of Neuroscience, University of Texas Southwestern Medical Center, 6000 Harry Hines Blvd., Dallas, TX 75390

<sup>4</sup> Department of Molecular Genetics, University of Texas Southwestern Medical Center, 6000 Harry Hines Blvd., Dallas, TX 75390

<sup>5</sup> Howard Hughes Medical Institute, University of Texas Southwestern Medical Center, 6000 Harry Hines Blvd., Dallas, TX 75390

### Abstract

RIM proteins play critical roles in synaptic vesicle priming and diverse forms of presynaptic plasticity. The C-terminal C<sub>2</sub>B domain is the only module that is common to all RIMs, but is only distantly related to well-studied C<sub>2</sub> domains, and its three-dimensional structure and interactions have not been characterized in detail. Using NMR spectroscopy, we now show that N- and C-terminal extensions beyond the predicted C<sub>2</sub>B domain core sequence are necessary to form a folded, stable RIM1 $\alpha$  C<sub>2</sub>B domain. We also find that the isolated RIM1 $\alpha$  C<sub>2</sub>B domain is not sufficient for previously described protein-protein interactions involving the RIM1 $\alpha$  C-terminus, suggesting that additional sequences adjacent to the C<sub>2</sub>B domain might be required for these interactions. On the other hand, analytical ultracentrifugation shows that the RIM1 $\alpha$  C<sub>2</sub>B domain forms weak dimers in solution. The crystal structure of the RIM1 $\alpha$  C<sub>2</sub>B domain dimer at 1.7 Å resolution reveals that it forms a  $\beta$ -sandwich characteristic of C<sub>2</sub> domains and that the unique N- and C-terminal extensions form a small subdomain that packs against the  $\beta$ -sandwich and mediates dimerization. Our results provide a structural basis to understand the function of RIM C<sub>2</sub>B domains and suggest that dimerization may be a crucial aspect of RIM function.

### Keywords

C<sub>2</sub> domain; RIM; neurotransmitter release; protein NMR; X-ray Crystallography

Synaptic vesicle exocytosis is central for interneuronal communication. This process involves several steps that include docking of synaptic vesicles at specialized sites of the plasma

<sup>†</sup>This work was supported by grant I-1304 from the Welch Foundation and NIH grant NS40944 to JR.

<sup>¶</sup>Structures have been deposited in the RCSB Protein Data Bank (PDB; <http://www.rcsb.org/pdb/>) (accession code XXX).

\*To whom correspondence should be addressed. Phone: 214-645-6360. FAX: 214-645-6353. E-mail: jose@arnie.swmed.edu.

<sup>1</sup>Abbreviations: NMR, nuclear magnetic resonance; HSQC, heteronuclear single quantum correlation; PKC, protein kinase C; RIM, Rab3-interacting molecule; SNARE, soluble N-ethylmaleimide sensitive factor attachment protein receptor; SNAP-25, synaptosomal associated protein of 25 kDa.

membrane called active zones, one or more priming reactions that leave the vesicles ready for release, and the actual release of neurotransmitters triggered by  $\text{Ca}^{2+}$  influx when an action potential reaches the presynaptic terminal (1). These different steps are governed by a complex protein machinery that shares several components with most other types of intracellular membrane traffic. These components include, among others, the soluble N-ethylmaleimide sensitive factor attachment protein receptors (SNAREs) synaptobrevin/VAMP, syntaxin and SNAP-25, which are critical for membrane fusion, and Rab3s, which are small GTPases from the Rab family that regulate neurotransmitter release (1–3). In addition, neurotransmitter release is controlled by proteins with specialized roles such as the  $\text{Ca}^{2+}$  sensor synaptotagmin 1 and the components of the active zone (3;4).

Presynaptic active zones are composed of a network of large proteins that include Liprins, Bassoon, piccolo/aczonin, RIMs, Munc13 and ELKS (5;6). Among these proteins, RIMs are particularly interesting because they exhibit multiple interactions that are believed to organize the active zone, and because they play multiple roles in regulating neurotransmitter release and presynaptic plasticity processes that mediate some forms of information processing in the brain (7). RIM1 $\alpha$  was initially identified as a large Rab3 effector that contains an N-terminal zinc finger (ZF) domain, a PDZ domain, and two C-terminal C<sub>2</sub> domains (the C<sub>2</sub>A and C<sub>2</sub>B domains) (8) (Fig. 1A). Three additional RIM genes were later identified in mammals (*RIM2*, *RIM3 $\gamma$*  and *RIM4 $\gamma$* ) (9;10), and one RIM homologue was found in *C. elegans* (*unc10*) (11). *RIM2* specifies a full-length transcript, RIM2 $\alpha$ , with an analogous domain structure to that of RIM1 $\alpha$ , a slightly shorter transcript that lacks the N-terminal ZF domain (RIM2 $\beta$ ), and a much shorter transcript (RIM2 $\gamma$ ) that only contains the C<sub>2</sub>B domain and adjacent sequences, similarly to RIM3 $\gamma$  and RIM4 $\gamma$  (Fig. 1A). Genetic ablation of *unc10* in *C. elegans* (11) or of RIM1 $\alpha$  and RIM2 $\alpha$  in mice (12) leads to a severe impairment in neurotransmitter release associated with a defect in synaptic vesicle priming. A milder phenotype is observed in RIM1 $\alpha$  knockout mice (13), indicating a partial functional redundancy of RIM1 $\alpha$  and RIM2 $\alpha$ . However, defects in short- and long-term presynaptic plasticity, as well as in memory and learning, are observed in the absence of RIM1 $\alpha$  (13–17), demonstrating the critical importance of this protein for brain function.

The proposed role of RIMs in organizing active zones emerged from the observation of diverse interactions involving their different domains (13). The N-terminal region of  $\alpha$ -RIMs including the ZF domain and adjacent sequences binds to Rab3 (8) and to Munc13-1 (18), a large active zone protein with a critical role in synaptic vesicle priming (19;20) that is executed by its MUN domain (21). Munc13-1 forms a homodimer through its N-terminal C<sub>2</sub>A domain (22), which is also involved in binding to the  $\alpha$ -RIM N-terminus (18) to yield a tripartite complex with Rab3 (23). Based on these results, it has been suggested that a Munc13-1 homodimer to Munc13-1/ $\alpha$ -RIM heterodimer switch may regulate synaptic vesicle priming and couple priming to some forms of presynaptic plasticity (22;23). Additional protein-protein interactions of  $\alpha$ -RIMs include those of a proline-rich sequence between the two C<sub>2</sub> domains with RIM binding proteins (9), and of its PDZ domain with ELKS (24), which provides an indirect link to the active zone proteins Piccolo and Bassoon (25). The RIM C<sub>2</sub>A domain was suggested to bind to SNAP-25 and synaptotagmin 1 (26), although these interactions could not be confirmed in separate studies (13;27). Finally, the RIM C<sub>2</sub>B domain has been reported to bind to liprins, which also form part of the active zone, and also to synaptotagmin 1 (13;26).

While until recently there was little information on the structure and interactions of RIM and munc13 domains, NMR and X-ray studies have uncovered in the last two years the structures of the RIM ZF domain (23) and C<sub>2</sub>A domain (27), the Munc13-1 C<sub>2</sub>A domain homodimer (22) and C<sub>1</sub> domain (28), the RIM ZF/Munc13-1 C<sub>2</sub>A domain heterodimer (22), and the RIM PDZ domain bound to an ELKS peptide (29). However, no detailed information is available on the structure and interactions of the RIM C<sub>2</sub>B domain. Both the high evolutionary sequence

conservation of the C<sub>2</sub>B domain (10) and its presence in all RIM isoforms (Fig. 1) suggest that this domain is critical for RIM function, which was supported by the finding that an Unc10 mutant lacking the C<sub>2</sub>B domain is unable to rescue unc10 function in *C. elegans* (11). C<sub>2</sub> domains are widespread protein modules whose most common properties are Ca<sup>2+</sup> and phospholipid binding (30). These properties have been extensively studied in archetypical C<sub>2</sub> domains such as those of synaptotagmin 1, which bind multiple Ca<sup>2+</sup> ions through five conserved aspartate residues (31–33). However, the RIM C<sub>2</sub>B domain is only distantly related to these C<sub>2</sub> domains (27) and does not contain a full complement of aspartate Ca<sup>2+</sup> ligands. Hence, the RIM C<sub>2</sub>B domain is unlikely to bind Ca<sup>2+</sup>, although this prediction has not been tested, and it is unclear whether this domain contains unusual structural features that may underlie a unique mechanism of action.

To shed light on these questions and provide a structural basis to understand the function of the RIM1 $\alpha$  C<sub>2</sub>B domain, we have analyzed its three-dimensional structure and interactions by NMR spectroscopy and X-ray crystallography. We find that N- and C-terminal extensions beyond the canonical C<sub>2</sub> domain sequence are required to form the complete, folded C<sub>2</sub>B domain of RIM1 $\alpha$ . We also find that the RIM1 $\alpha$  C<sub>2</sub>B domain does not bind Ca<sup>2+</sup> and is not sufficient to bind to the synaptotagmin 1 C<sub>2</sub> domains or to liprins, but forms a dimer in solution. The crystal structure of the RIM1 $\alpha$  C<sub>2</sub>B domain using diffraction data to 1.7 Å reveals a  $\beta$ -sandwich structure that is similar to those of other C<sub>2</sub> domains but includes in addition a subdomain formed by the N- and C-terminal extensions, which pack against one side of the  $\beta$ -sandwich and mediate dimerization. Our results suggest a model whereby one of the functions of the RIM C<sub>2</sub>B domain may entail dimerization to facilitate the Munc13-1 C<sub>2</sub>A domain homodimer to Munc13-1/ $\alpha$ -RIM heterodimer switch that likely regulates synaptic vesicle priming.

## EXPERIMENTAL PROCEDURES

### Sample preparation

DNA plasmids encoding GST fusion proteins of diverse fragments of rat RIM1 $\alpha$  spanning the C<sub>2</sub>B domain (see Figure 1B) were made using custom-designed primers and standard PCR cloning techniques, and subcloned into the pGEX-KT expression vector (34). The fusion proteins were expressed at 23°C in *E. coli* BL21, isolated by affinity chromatography on glutathione-sepharose followed by on-resin cleavage with thrombin. The eluted proteins were further purified by gel filtration chromatography on an S75 column (Pharmacia). Uniform <sup>15</sup>N- labeling was achieved by growing the bacteria in <sup>15</sup>NH<sub>4</sub>Cl as the sole nitrogen sources. The seleno-methionine derivative of rat RIM1 $\alpha$  C<sub>2</sub>B domain was purified similarly. Fragments corresponding to the rat synaptotagmin 1 C<sub>2</sub>A domain (residues 140–267), C<sub>2</sub>B domain (residues 271–421) and C<sub>2</sub>AB domains (residues 140–421), as well as a rat  $\alpha$ -liprin3 fragment spanning the minimal RIM-binding region (residues 183–470) were expressed and purified as described previously (13;32;33;35).

### NMR spectroscopy

All NMR data were acquired at 27 °C on Varian INOVA500 or INOVA600 spectrometers (Varian, Palo Alto, California, USA) with RIM1 $\alpha$  C<sub>2</sub> domain samples dissolved in standard buffer [20 mM MES (pH 6.0), 150 mM NaCl, 1 mM EDTA, 0.5 mM TCEP], using H<sub>2</sub>O/D<sub>2</sub>O 95:5 (v/v) as the solvent. The 1D <sup>1</sup>H NMR spectra were acquired at 2+ variable RIM1 $\alpha$  C<sub>2</sub>B domain concentrations (12  $\mu$ M to 1.22 mM) using water presaturation. Ca<sup>2+</sup> titrations monitored by <sup>1</sup>H-<sup>15</sup>N HSQC spectra were performed as described (32). All 2D <sup>1</sup>H-<sup>15</sup>N HSQC spectra were acquired at 80–100  $\mu$ M protein concentrations. The 1D <sup>15</sup>N-edited <sup>1</sup>H NMR experiments to test for lipid binding were performed with 5  $\mu$ M RIM1 $\alpha$  C<sub>2</sub>B domain by

acquiring the first trace of a  $^1\text{H}$ - $^{15}\text{N}$  HSQC spectrum. All NMR data were processed with the program NMRPipe (36) and analyzed with the program NMRView (37).

### FRET assays

Emission fluorescence spectra were acquired on a PTI spectrometer with excitation at 285 nm. with samples containing 1  $\mu\text{M}$  RIM1 $\alpha$  C<sub>2</sub>B domain and/or 0.01 mg/ml phospholipid vesicles composed of 65% phosphatidylcholine (PC), 25% phosphatidylserine (PS) and 10% dansyl-phosphatidylethanolamine (dansyl-PE), dissolved in standard buffer containing 1 mM EDTA or 1 mM  $\text{CaCl}_2$ .

### X-ray crystallography

Rat RIM1 $\alpha$  C<sub>2</sub>B domain dissolved in 20 mM MES (pH 6.0), 150 mM NaCl, 1 mM EDTA and 0.5 mM TCEP was concentrated to 19 mg/mL for crystallization using the hanging drop vapor diffusion method. Drops in a ratio of 1  $\mu\text{l}$  protein to 1  $\mu\text{l}$  well solution were equilibrated against 0.1 M sodium citrate (pH 4.1), 1.55 M  $(\text{NH}_4)_2\text{SO}_4$  at 20°C. Crystals appeared overnight and grew to a final size of  $0.05 \times 0.05 \times 0.05$  mm within two days. Prior to data collection, crystals were transferred into a solution of 0.1 M sodium citrate (pH 4.1), 0.15 M NaCl, 1.7 M  $(\text{NH}_4)_2\text{SO}_4$ , and 20% (v/v) ethylene glycol, and then flash cooled in liquid propane. Selenomethionine-derivatized (SeMet) crystals were grown and cryoprotected via a similar procedure to wild type, and equilibrated against 0.1 M Sodium Citrate (pH 3.5), 1.75 M  $(\text{NH}_4)_2\text{SO}_4$  and cryoprotected in a solution of 0.1 M Sodium Citrate (pH 3.5), 0.15 M NaCl, 1.9 M  $(\text{NH}_4)_2\text{SO}_4$ , and 20% ethylene glycol. Diffraction data were collected at the Structural Biology Center beamline 19BM of the Advanced Photon Source (Argonne National Laboratory, Argonne, Illinois, USA) at 100K to a Bragg spacing ( $d_{\text{min}}$ ) of 1.73 Å. The crystals exhibited the symmetry of space group  $\text{P}3_121$  with unit cell parameters of  $a = b = 62.0$  Å,  $c = 145.2$  Å, and contained two molecules per asymmetric unit. Data were processed and scaled in the HKL2000 program suite (38). The rat RIM1- $\alpha$  C<sub>2</sub>B domain structure was determined with experimental phases obtained from a single-wavelength anomalous dispersion (SAD) experiment using x-rays with energy near the selenium K absorption edge. Using data to 1.73 Å, 9 of 10 possible selenium sites were located using the program *SHELXD* (39) and refined with the program *MLPHARE* (40), resulting in a figure of merit of 0.348. Phases were improved by density modification in the program *DM* (41), resulting in a final overall figure of merit of 0.828 in the last resolution shell (1.78-1.73 Å). Refinement of the model was carried out with the program Refmac5 (42) of the CCP4 package (43). Manual adjustments to the model were carried out with the programs O (44) and Coot (45). The electron density clearly showed the presence of seven sulfate ions. After refinement of the protein part was complete, solvent molecules were added where stereochemically reasonable. The model has good stereochemistry, with 88.0% of residues in the most favored region of the Ramachandran plot and none in disallowed regions. Data collection and refinement statistics are listed in Table 1.

### Analytical ultracentrifugation

Sedimentation equilibrium experiments were performed with a Beckman Optima XL-I analytical ultracentrifuge using a 4-position An60Ti rotor and an absorbance optical system (Beckman Instruments, Fullerton, California, USA). Each cell has a six-channel carbon-Epon centerpiece with two quartz windows giving an optical path length of 1.2 cm. The sample channels and reference channels were filled with 100  $\mu\text{l}$  protein solutions and 110  $\mu\text{l}$  buffer solutions, respectively. Absorbance was monitored for each cell in 0.002 cm steps at a wavelength of 280 nm. Samples were centrifuged at 20,000 rpm, 25,000 rpm, 29,000 rpm, and 35,000 rpm at 4 °C until equilibrium was reached, followed by overspeed runs at 42,000 rpm to obtain baseline values of absorbance that were used in subsequent fits. The loading concentration of RIM1 $\alpha$  C<sub>2</sub>B domain was 22 $\mu\text{M}$  in 20 mM MES (pH 6.0), 150 mM NaCl, 1

mM EDTA and 0.5mM TCEP. The partial specific volumes of RIM1 $\alpha$  C2B domain at 4 °C was calculated from its amino acid composition to be 0.7362 cm<sup>3</sup>·g<sup>-1</sup>, and the monomeric molecular mass was calculated to be 18,758.9 Da. The solvent density was calculated to be 1.007 g·ml<sup>-1</sup> at 4 °C. Data sets were fitted to either the single ideal species model or the self-association model using Beckman Optima XL-A/XL-I data analysis software (Origin 6.03). Global analysis was applied to data sets obtained at the different rotor speeds.

## RESULTS

### Definition of the RIM1 $\alpha$ C<sub>2</sub>B domain boundaries

All C<sub>2</sub> domains whose three-dimensional structure has been determined are formed largely by sequences that adopt a  $\beta$ -sandwich with loops and sometimes  $\alpha$ -helices emerging at the top and the bottom of the sandwich. Some C<sub>2</sub> domains contain extensions in their termini that provide additional structural elements [e.g. the C<sub>2</sub>B domain of synaptotagmin 1 (33) or the Munc13-1 C<sub>2</sub>A domain (22)]. To investigate the minimal sequence of RIM1 $\alpha$  required to form a folded C<sub>2</sub>B domain, we prepared six constructs to express RIM1 $\alpha$  fragments spanning the predicted C<sub>2</sub>B domain signature with or without N-and/or C-terminal extensions (C2B-1 to C2B-6; see Fig. 1B). All these fragments could be expressed in bacteria, but only those containing an extension to the very C-terminus of RIM1 $\alpha$  were soluble. The presence of N-terminal extensions of different lengths did not appear to affect the solubility of these fragments, but complete deletion of the N-terminal sequence extensions led to instability and low yields during purification (C2B-5 fragment; Fig. 1B).

We previously have shown that <sup>1</sup>H-<sup>15</sup>N heteronuclear single quantum coherence (HSQC) spectra provide a useful tool to examine the behavior and proper folding of protein fragments, which can guide crystallization trials (22;46;47). Hence, we acquired <sup>1</sup>H-<sup>15</sup>N HSQC spectra of the two RIM1 $\alpha$  fragments that were soluble and could be purified in high yields (C2B-1 and C2B-3; Fig. 1B). The <sup>1</sup>H-<sup>15</sup>N HSQC spectrum of the C2B-1 fragment exhibited abundant cross-peaks in the center of the spectrum and only a few very broad cross-peaks in well-resolved regions (Fig. 2A); such cross-peak broadening likely arises from aggregation. However, the <sup>1</sup>H-<sup>15</sup>N HSQC spectrum of the C2B-3 fragment exhibited much narrower cross-peaks and excellent dispersion (Fig. 2B), showing that this fragment is properly folded and well-behaved. These results show that the C2B-3 fragment spans the minimal sequence for proper folding, and hereafter we will refer to this fragment as the RIM1 $\alpha$  C<sub>2</sub>B domain.

### Analysis of RIM1 $\alpha$ C<sub>2</sub>B domain interactions

<sup>1</sup>H-<sup>15</sup>N HSQC spectra also provide a powerful tool to analyze binding of ions to proteins, as well as protein-protein interactions. Thus, we tested whether the RIM1 $\alpha$  C<sub>2</sub>B domain binds Ca<sup>2+</sup> by acquiring <sup>1</sup>H-<sup>15</sup>N HSQC spectra in the absence and presence of Ca<sup>2+</sup>. Even Ca<sup>2+</sup> concentrations as high as 10 mM caused practically no perturbation in the <sup>1</sup>H-<sup>15</sup>N HSQC spectrum of RIM1 $\alpha$  C<sub>2</sub>B domain (Fig. 3A), showing that, as predicted, this domain is unable to bind Ca<sup>2+</sup>. We also used a fluorescence resonance energy transfer (FRET) assay (33) to test for phospholipid binding to the RIM1 $\alpha$  C<sub>2</sub>B domain in the absence or presence of Ca<sup>2+</sup>, but no binding was observed (Fig. 4A). These FRET assays commonly detect phospholipid binding to Ca<sup>2+</sup>-dependent C<sub>2</sub> domains because at least one tryptophan is close to the membrane in their usual Ca<sup>2+</sup>-induced phospholipid bound orientation. Since the RIM1 $\alpha$  C<sub>2</sub>B domain could potentially bind to phospholipids in a different orientation that could yield minimal FRET, we also tested for phospholipid binding using 1D <sup>15</sup>N edited <sup>1</sup>H NMR spectra of 5  $\mu$ M <sup>15</sup>N-labeled RIM1 $\alpha$  C<sub>2</sub>B domain. In these spectra, a strong reduction of the signal intensities is expected upon binding to a large unlabeled target such as phospholipid vesicles (23;48). However, no significant perturbations were observed upon addition of phospholipids in the absence or presence of Ca<sup>2+</sup> (Fig. 4B), confirming the FRET results.



The RIM1 $\alpha$  C<sub>2</sub>B domain was reported to bind to synaptotagmin 1 (13;26), an interaction that could be critical for RIM function given the demonstrated role of synaptotagmin 1 as a Ca<sup>2+</sup> sensor in neurotransmitter release (49;50). Hence, we attempted to analyze this interaction using NMR spectroscopy and a synaptotagmin 1 fragment that spans most of its cytoplasmic region and contains its two C<sub>2</sub> domains (C<sub>2</sub>AB fragment). However, addition of an excess of unlabeled C<sub>2</sub>AB fragment to <sup>15</sup>N-labeled RIM1 $\alpha$  C<sub>2</sub>B domain caused almost no perturbation in the <sup>1</sup>H-<sup>15</sup>N HSQC spectrum of the latter in the absence or presence of 10 mM Ca<sup>2+</sup> (Fig. 3B,C). Analogous results were obtained when we recorded <sup>1</sup>H-<sup>15</sup>N HSQC spectra of <sup>15</sup>N-labeled synaptotagmin 1 C<sub>2</sub>A domain or C<sub>2</sub>B domain in the absence or presence of unlabeled RIM1 $\alpha$  C<sub>2</sub>B domain (data not shown). It is important to note that <sup>1</sup>H-<sup>15</sup>N HSQC spectra are highly sensitive to protein-protein interactions and that all these data were acquired with soluble, properly folded fragments that are well-characterized by spectroscopic techniques. Hence, these results clearly establish that the isolated RIM1 $\alpha$  C<sub>2</sub>B domain does not form binary complexes with the synaptotagmin 1 C<sub>2</sub> domains at the protein concentrations used in these experiments (ca. 100  $\mu$ M), and suggest that sequences beyond the RIM1 $\alpha$  C<sub>2</sub>B domain and/or the synaptotagmin 1 C<sub>2</sub> domains may be required for direct interactions between these proteins. Using <sup>1</sup>H-<sup>15</sup>N HSQC spectra, we were also unable to observe any interaction between <sup>15</sup>N-labeled RIM1 $\alpha$  C<sub>2</sub>B domain and an unlabeled liprin fragment that was identified as the RIM-binding region of liprins (13), suggesting again that the RIM1 $\alpha$  C<sub>2</sub>B domain is not sufficient for these previously described interactions, which thus may require additional RIM1 $\alpha$  sequences preceding the C<sub>2</sub>B domain.

During our NMR analyses of the RIM1 $\alpha$  C<sub>2</sub>B domain, we observed that the resonance line widths were concentration dependent. The resonance broadening is illustrated by the signals from well-resolved methyl groups in the 1D <sup>1</sup>H NMR spectra of 20  $\mu$ M, 101  $\mu$ M and 406  $\mu$ M RIM1 $\alpha$  C<sub>2</sub>B domain shown in Figure 5A. Note that the vertical scale of the spectra was normalized for the different protein concentrations, and the resonance broadening is thus manifested not only by the increasing line widths but also by the decreasing intensities at higher protein concentrations. The measured methyl line widths (after subtracting 7 Hz due to the homonuclear coupling with the neighboring methine proton) ranged from 6–7 Hz at 12  $\mu$ M RIM1 $\alpha$  C<sub>2</sub>B domain, as expected for a monomeric species, to 12–14 Hz at 1.22 mM RIM1 $\alpha$  C<sub>2</sub>B domain. These results indicated that the RIM1 $\alpha$  C<sub>2</sub>B domain dimerizes in solution. To confirm this conclusion, we used analytical ultracentrifugation. Indeed, equilibrium sedimentation data did not correspond to a monomeric species but could be fitted well to a monomer-dimer equilibrium with a dissociation constant of  $96.3 \pm 17.5$   $\mu$ M (Fig. 5B). This result is consistent with the observed NMR line widths and demonstrates that the RIM1 $\alpha$  C<sub>2</sub>B domain forms weak dimers in solution.

### Crystal structure of the RIM1 $\alpha$ C<sub>2</sub>B domain dimer

Based on the good quality of the <sup>1</sup>H-<sup>15</sup>N HSQC spectra of the RIM1 $\alpha$  C<sub>2</sub>B domain (Fig. 2B), and following our generally philosophy of using <sup>1</sup>H-<sup>15</sup>N HSQC spectra as a guide for protein crystallization (22;46), we initiated crystallization trials of the RIM1 $\alpha$  C<sub>2</sub>B domain (fragment C2B-3) and quickly obtained high quality crystals in 0.1 M sodium citrate (pH 4.1), 1.55 M (NH<sub>4</sub>)<sub>2</sub>SO<sub>4</sub>. Because molecular replacement attempts were unsuccessful, the crystal structure of the RIM1 $\alpha$  C<sub>2</sub>B domain was determined by the single-wavelength anomalous dispersion (SAD) method and refined using data to 1.7 Å resolution. A representative region of the electron density is shown in Figure 6A, and Table 1 summarizes the data collection and refinement statistics.

In agreement with the equilibrium sedimentation data, the RIM1 $\alpha$  C<sub>2</sub>B domain forms a symmetric dimer in the crystals. A ribbon diagram of one of the monomers is represented in Figure 6B, and a superposition of both monomers (Figure 6C) shows that they are almost

identical (0.31 Å rms deviation between all common heavy atoms). The structure contains a  $\beta$ -sandwich formed by two four-stranded  $\beta$ -sheets that is characteristic of C<sub>2</sub> domains (30) and encompasses the portion of the RIM1 $\alpha$  C<sub>2</sub>B domain that exhibits homology to the C<sub>2</sub> domain family (residues 1462–1582). The N- and C-terminal extensions beyond this region form a small subdomain that packs against a largely hydrophobic side of the  $\beta$ -sandwich and includes two separate helical turns and a short, two-stranded antiparallel  $\beta$ -sheet (strands 1 and 10). Such hydrophobic packing may explain the necessity of these N- and C-terminal extensions for the proper folding and/or stability of the RIM1 $\alpha$  C<sub>2</sub>B domain. Strands 1 and 10 are provided by the very N- and C-termini of the RIM1 $\alpha$  C<sub>2</sub>B domain, and the strand-strand interaction helps to bring the two termini in close proximity. Note that the loop connecting the short N-terminal strand (strand 1 in Figs. 6B,C) to the first strand of the  $\beta$ -sandwich (strand 2 in Figs. 6B,C) is partially disordered in one of the monomers (in blue in Fig. 6C). Partial disorder is also observed in the loops emerging at the top of the  $\beta$ -sandwich that commonly bind Ca<sup>2+</sup> in C<sub>2</sub> domains, but not in the case of the RIM1 $\alpha$  C<sub>2</sub>B domain (loops 1–3; Figs. 6B,C). Several sulfate ions bound to clusters of basic residues of the RIM1 $\alpha$  C<sub>2</sub>B domain were observed in the electron density (e.g. Fig. 6A). It is unclear whether this finding arises from potential functional activities of these clusters or from the high concentration of sulfate ions in the crystallization conditions.

A structural comparison using the program DALI (51) revealed that, as expected, the structure of the RIM1 $\alpha$  C<sub>2</sub>B domain is similar to those of all C<sub>2</sub> domains deposited in the Protein Data Bank (PDB). The highest Z score yielded by DALI corresponded to the synaptotagmin 1 C<sub>2</sub>A domain (1.65 Å rms deviation between 115 common C $\beta$  carbons). The superposition of ribbon diagrams of the RIM1 $\alpha$  C<sub>2</sub>B domain and the synaptotagmin 1 C<sub>2</sub>A domain shown in Figure 6D illustrates the close structural similarity of their  $\beta$ -sandwiches despite their low sequence identity (21% using standard sequence alignment tools; 27% using the structure-based sequence alignment yielded by DALI). The superposition also illustrates that the most prominent difference between these two C<sub>2</sub> domains is the subdomain formed by the N- and C-terminal extensions of the RIM1 $\alpha$  C<sub>2</sub>B domain. It is noteworthy that, although most C<sub>2</sub> domains only contain the  $\beta$ -sandwich, the synaptotagmin 1 C<sub>2</sub>B domain (33) and the Munc13-1 C<sub>2</sub>A domain (22) provide two examples exhibiting additional structural elements that emerge at the same side of the  $\beta$ -sandwich where the unique subdomain of the RIM1 $\alpha$  C<sub>2</sub>B domain is located (a C-terminal  $\alpha$ -helix in the synaptotagmin 1 C<sub>2</sub>B domain and a  $\beta$ -hairpin formed by a long loop sequence in the Munc13-1 C<sub>2</sub>A domain).

The two monomers of the RIM1 $\alpha$  C<sub>2</sub>B domain dimer are related by a two-fold axis (parallel to the vertical axis in the orientation of Figure 7A). The total surface area buried by dimerization is 900 Å<sup>2</sup>. Interestingly, the dimer interface is largely formed by the subdomains encompassing the N- and C-terminal extensions of each monomer. The subdomains from each monomer pack against each other and against the concave surface formed by strands 4, 5, 7 and 8 of the  $\beta$ -sandwich from the opposite monomer. The close-up of the dimer interface shown in Figure 7B reveals that contacts between the two monomers involve a number of hydrophobic and polar interactions, including a salt bridge between K1513 of one monomer and D1589 of the opposing monomer. A map of the electrostatic potential on the surface of the dimer exhibits a striking dipolar character, with the top half being largely positive and the bottom half largely negative (Fig. 7C). A clear dipolar character was also observed in the RIM1 $\alpha$  C<sub>2</sub>A domain (27). This feature of the RIM C<sub>2</sub> domains may have functional significance, but further research will be required to assess this possibility.

Figure 8 shows a sequence alignment of RIM C<sub>2</sub>B domains from different species, the rat RIM1 $\alpha$  C<sub>2</sub>A domain, and diverse Ca<sup>2+</sup>-binding C<sub>2</sub> domains whose structures have been previously solved, including those of synaptotagmin 1, PKCs and rabphilin. The alignment illustrates the very high sequence conservation of RIM C<sub>2</sub>B domains. Some of the conserved



residues are shared with C<sub>2</sub> domains in general, whereas many other residues are selectively conserved in RIM C<sub>2</sub>B domains. The alignment also illustrates how the Ca<sup>2+</sup>-binding C<sub>2</sub> domains are distantly related to both RIM C<sub>2</sub> domains, which at the same time are also distantly related to each other [see (27) for a more detailed analysis]. In general, residues involved in dimerization of the RIM1 $\alpha$  C<sub>2</sub>B domain are highly conserved, although those belonging to the C-terminal extension are less conserved in invertebrates (Figure 8), suggesting that dimerization may only occur in vertebrate RIMs.

## DISCUSSION

RIMs constitute a fascinating family of proteins that play crucial roles in regulating synaptic neurotransmitter release and different forms of presynaptic plasticity, acting also as scaffolds to organize the active zone. Among the different domains found in the different RIM isoforms, only the C<sub>2</sub>B domain is present in all of them, suggesting that this domain is a key determinant of RIM function. This notion is also supported by the high evolutionary conservation of the RIM C<sub>2</sub>B domain sequence and by rescue experiments of Unc10 mutants in *C. elegans* (11). To provide a basis for understanding the function of the RIM1 $\alpha$  C<sub>2</sub>B domain, here we have analyzed its three-dimensional structure and interactions with diverse targets using NMR spectroscopy and X-ray crystallography. Our results define the boundaries of the RIM1 $\alpha$  C<sub>2</sub>B domain, showing that N- and C-terminal extensions are necessary to form a folded, stable module. We find that the RIM1 $\alpha$  C<sub>2</sub>B domain does not bind Ca<sup>2+</sup>, as predicted from the fact that this domain contains only one of the five canonical aspartate residues that commonly form the Ca<sup>2+</sup> binding sites of C<sub>2</sub> domains (see Fig. 8). We were unable to verify previously described protein-protein interactions involving the RIM1 $\alpha$  C<sub>2</sub>B domain, but we uncovered a novel interaction, dimerization, that may be important for its function. The crystal structure of the RIM1 $\alpha$  C<sub>2</sub>B domain reveals how its signature C<sub>2</sub>-domain sequence forms a  $\beta$ -sandwich characteristic of C<sub>2</sub> domains, and how the N- and C-terminal extensions form a subdomain that packs against a hydrophobic side of the  $\beta$ -sandwich. This structure constitutes only the second three-dimensional structure described for a C<sub>2</sub> domain dimer, and the major participation of the unusual subdomain in dimerization suggests that C<sub>2</sub> domains may be able to act as protein-protein interaction domains by diverse mechanisms.

Our sedimentation equilibrium data show that dimerization of the RIM1 $\alpha$  C<sub>2</sub>B domain is characterized by a relatively weak affinity. However, the dimeric structure observed in the crystals of the RIM1 $\alpha$  C<sub>2</sub>B domain shows that dimerization arises from specific interactions involving the concave surface of the  $\beta$ -sandwich and the subdomain formed by the N- and C-terminal extensions. Moreover, it is plausible that dimerization may be strengthened by sequences N-terminal to the C<sub>2</sub>B domain or by other protein-protein interactions that participate in organizing the active zone and may increase the local concentration of RIMs. Furthermore, the formation of RIM dimers could provide a mechanism to facilitate the Munc13-1 homodimer to Munc13-1/ $\alpha$ -RIM heterodimer switch that is likely to play a key role in synaptic vesicle priming (22), because the RIM dimer could engage two Munc13-1 molecules during the switch (Fig. 9). Clearly, further research will be necessary to assess the physiological relevance of the dimerization of the RIM1 $\alpha$  C<sub>2</sub>B domain, but our data raise the possibility that dimerization may be a key aspect of RIM function and the crystal structure of the RIM1 $\alpha$  C<sub>2</sub>B domain described here will facilitate the design of mutagenesis experiments to test this notion.

Two previous studies reported interactions between the RIM1 $\alpha$  C<sub>2</sub>B domain and synaptotagmin 1 (13;26). Since the synaptotagmin 1 C<sub>2</sub> domains form most of its cytoplasmic region and are largely responsible for synaptotagmin 1 function (1;3;4), it was surprising that we could not detect an interaction between the synaptotagmin 1 C<sub>2</sub>AB fragment and the RIM1 $\alpha$  C<sub>2</sub>B domain. Because our data were obtained in solution with well-folded proteins that

were well characterized by spectroscopic techniques, and because  $^1\text{H}$ - $^{15}\text{N}$  HSQC provides a very sensitive tool to detect protein-protein interactions, our data conclusively show that at least these recombinant RIM1 $\alpha$  and synaptotagmin 1 fragments expressed in bacteria do not form binary complexes in the absence or presence of  $\text{Ca}^{2+}$ . It is noteworthy that in previous studies of the RIM2 C<sub>2</sub>A domain by NMR spectroscopy (27), we were also unable to detect previously described interactions of this domain with SNAP-25 and synaptotagmin 1 (26). It is plausible that these contradictions arise in part because some of the previous data were obtained with GST-pulldown experiments, which are prone to artifacts. However, it is also possible that RIM1 $\alpha$ /synaptotagmin 1 interactions require RIM1 $\alpha$  sequences adjacent to its C<sub>2</sub> domains. Note also that we did not detect binding between the isolated RIM1 $\alpha$  C<sub>2</sub>B domain and a liprin fragment containing the minimal RIM-binding sequence, but the RIM/liprin interaction appears to be tight (13) and is likely to be functionally significant (7). Hence, sequences preceding the RIM1 $\alpha$  C<sub>2</sub>B domain may also be necessary for liprin binding. These results emphasize the need for further research including the sequences adjacent to the RIM C<sub>2</sub> domains to fully understand their biochemical and functional properties.

Our results also have implications for our overall understanding of how C<sub>2</sub> domains function. Initial studies of these widespread protein modules suggested that they generally function as  $\text{Ca}^{2+}$ -dependent phospholipid binding domains that exhibit little  $\text{Ca}^{2+}$ -induced structural changes (30). However, as more C<sub>2</sub> domains are being studied, more examples are found that deviate from this paradigm. For instance, the Piccolo C<sub>2</sub>A domain exhibits a drastic  $\text{Ca}^{2+}$ -induced conformational change (52), and the rat synaptotagmin 4 C<sub>2</sub>B domain does not bind  $\text{Ca}^{2+}$  despite containing a full complement of potential  $\text{Ca}^{2+}$  ligands (47). Recently, the crystal structures of the Munc13-1 C<sub>2</sub>A domain homodimer and of the Munc13-1 C<sub>2</sub>A domain/RIM2 $\alpha$  ZF domain heterodimer (22) provided a first glimpse at atomic resolution of how a C<sub>2</sub> domain engages in protein-protein interactions. The crystal structure of the RIM1 $\alpha$  C<sub>2</sub>B domain described here now reveals the nature of a second C<sub>2</sub> domain dimer at atomic resolution. Although Munc13-1 C<sub>2</sub>A domain dimerization also involved the concave sheet of the  $\beta$ -sandwich, the mode of dimerization involved formation of a  $\beta$ -barrel between the concave sheet of each monomer (22) and is thus different from the dimerization mode of the RIM1 $\alpha$  C<sub>2</sub>B domain. Hence, the novel mode of dimerization of the RIM1 $\alpha$  C<sub>2</sub>B domain suggests that C<sub>2</sub> domains may be able to dimerize and participate in protein-protein interactions by a variety of mechanisms. It appears that we are just starting to uncover this diversity.

## Acknowledgements

Results shown in this report are derived in part from work performed at Argonne National Laboratory, Structural Biology Center at the Advanced Photon Source. Argonne is operated by UChicago Argonne, LLC, for the U.S. Department of Energy, Office of Biological and Environmental Research under contract DE-AC02-06CH11357.

## References

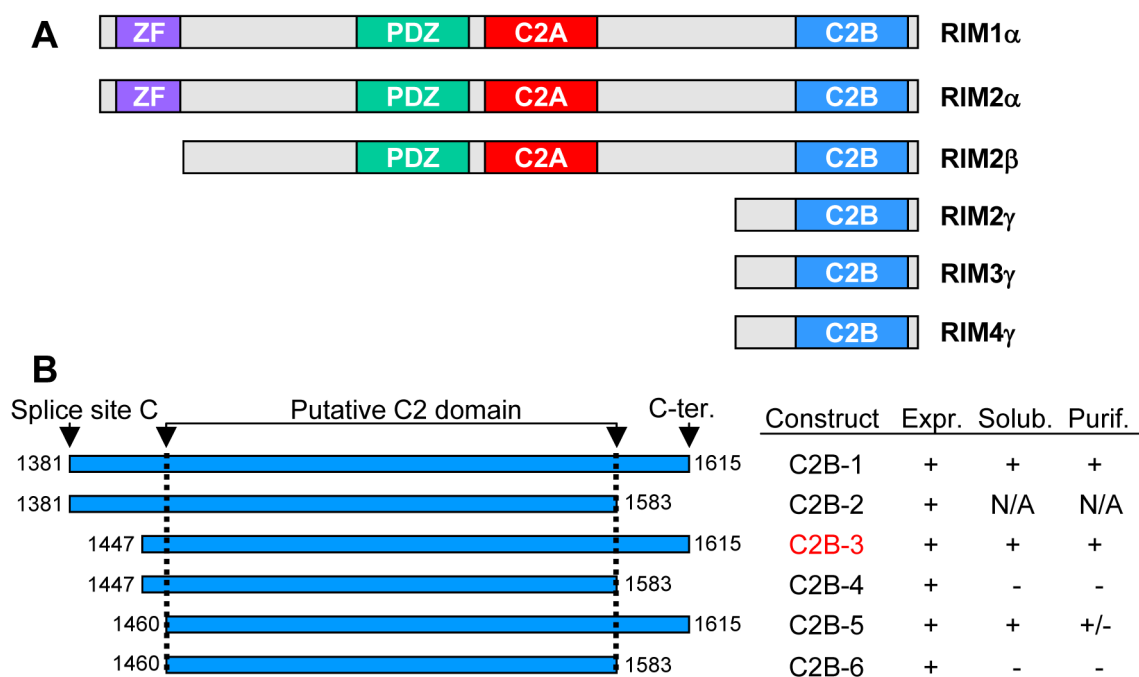
1. Sudhof TC. The synaptic vesicle cycle. *Annu Rev Neurosci* 2004;27:509–547. [PubMed: 15217342]
2. Jahn R, Scheller RH. SNAREs--engines for membrane fusion. *Nat Rev Mol Cell Biol* 2006;7:631–643. [PubMed: 16912714]
3. Rizo J, Chen X, Arac D. Unraveling the mechanisms of synaptotagmin and SNARE function in neurotransmitter release. *Trends Cell Biol* 2006;16:339–350. [PubMed: 16698267]
4. Bai J, Chapman ER. The C2 domains of synaptotagmin--partners in exocytosis. *Trends Biochem Sci* 2004;29:143–151. [PubMed: 15003272]
5. Garner CC, Kindler S, Gundelfinger ED. Molecular determinants of presynaptic active zones. *Curr Opin Neurobiol* 2000;10:321–327. [PubMed: 10851173]
6. Rosenmund C, Rettig J, Brose N. Molecular mechanisms of active zone function. *Curr Opin Neurobiol* 2003;13:509–519. [PubMed: 14630212]

7. Kaeser PS, Sudhof TC. RIM function in short- and long-term synaptic plasticity. *Biochem Soc Trans* 2005;33:1345–1349. [PubMed: 16246115]
8. Wang Y, Okamoto M, Schmitz F, Hofmann K, Sudhof TC. Rim is a putative Rab3 effector in regulating synaptic-vesicle fusion. *Nature* 1997;388:593–598. [PubMed: 9252191]
9. Wang Y, Sugita S, Sudhof TC. The RIM/NIM family of neuronal C2 domain proteins. Interactions with Rab3 and a new class of Src homology 3 domain proteins. *J Biol Chem* 2000;275:20033–20044. [PubMed: 10748113]
10. Wang Y, Sudhof TC. Genomic definition of RIM proteins: evolutionary amplification of a family of synaptic regulatory proteins( small star, filled ). *Genomics* 2003;81:126–137. [PubMed: 12620390]
11. Koushika SP, Richmond JE, Hadwiger G, Weimer RM, Jorgensen EM, Nonet ML. A post-docking role for active zone protein Rim. *Nat Neurosci* 2001;4:997–1005. [PubMed: 11559854]
12. Schoch S, Mittelstaedt T, Kaeser PS, Padgett D, Feldmann N, Chevaleyre V, Castillo PE, Hammer RE, Han W, Schmitz F, Lin W, Sudhof TC. Redundant functions of RIM1alpha and RIM2alpha in Ca(2+)-triggered neurotransmitter release. *EMBO J* 2006;25:5852–5863. [PubMed: 17124501]
13. Schoch S, Castillo PE, Jo T, Mukherjee K, Geppert M, Wang Y, Schmitz F, Malenka RC, Sudhof TC. RIM1alpha forms a protein scaffold for regulating neurotransmitter release at the active zone. *Nature* 2002;415:321–326. [PubMed: 11797009]
14. Castillo PE, Schoch S, Schmitz F, Sudhof TC, Malenka RC. RIM1alpha is required for presynaptic long-term potentiation. *Nature* 2002;415:327–330. [PubMed: 11797010]
15. Lonart G, Schoch S, Kaeser PS, Larkin CJ, Sudhof TC, Linden DJ. Phosphorylation of RIM1 alpha by PKA triggers presynaptic long-term potentiation at cerebellar parallel fiber synapses. *Cell* 2003;115:49–60. [PubMed: 14532002]
16. Calakos N, Schoch S, Sudhof TC, Malenka RC. Multiple roles for the active zone protein RIM1 alpha in late stages of neurotransmitter release. *Neuron* 2004;42:889–896. [PubMed: 15207234]
17. Powell CM, Schoch S, Monteggia L, Barrot M, Matos MF, Feldmann N, Sudhof TC, Nestler EJ. The presynaptic active zone protein RIM1alpha is critical for normal learning and memory. *Neuron* 2004;42:143–153. [PubMed: 15066271]
18. Betz A, Thakur P, Junge HJ, Ashery U, Rhee JS, Scheuss V, Rosenmund C, Rettig J, Brose N. Functional interaction of the active zone proteins Munc13-1 and RIM1 in synaptic vesicle priming. *Neuron* 2001;30:183–196. [PubMed: 11343654]
19. Augustin I, Rosenmund C, Sudhof TC, Brose N. Munc13-1 is essential for fusion competence of glutamatergic synaptic vesicles. *Nature* 1999;400:457–461. [PubMed: 10440375]
20. Varoqueaux F, Sigler A, Rhee JS, Brose N, Enk C, Reim K, Rosenmund C. Total arrest of spontaneous and evoked synaptic transmission but normal synaptogenesis in the absence of Munc13-mediated vesicle priming. *Proc Natl Acad Sci U S A* 2002;99:9037–9042. [PubMed: 12070347]
21. Basu J, Shen N, Dulubova I, Lu J, Guan R, Guryev O, Grishin NV, Rosenmund C, Rizo J. A minimal domain responsible for Munc13 activity. *Nat Struct Mol Biol* 2005;12:1017–1018. [PubMed: 16228007]
22. Lu J, Machius M, Dulubova I, Dai H, Sudhof TC, Tomchick DR, Rizo J. Structural Basis for a Munc13-1 Homodimer to Munc13-1/RIM Heterodimer Switch. *PLoS Biol* 2006;4:e192. [PubMed: 16732694]
23. Dulubova I, Lou X, Lu J, Huryeva I, Alam A, Schneggenburger R, Sudhof TC, Rizo J. A Munc13/ RIM/Rab3 tripartite complex: from priming to plasticity? *EMBO J* 2005;24:2839–2850. [PubMed: 16052212]
24. Wang Y, Liu X, Biederer T, Sudhof TC. A family of RIM-binding proteins regulated by alternative splicing: Implications for the genesis of synaptic active zones. *Proc Natl Acad Sci U S A* 2002;99:14464–14469. [PubMed: 12391317]
25. Takao-Rikitsu E, Mochida S, Inoue E, guchi-Tawarada M, Inoue M, Ohtsuka T, Takai Y. Physical and functional interaction of the active zone proteins, CAST, RIM1, and Bassoon, in neurotransmitter release. *J Cell Biol* 2004;164:301–311. [PubMed: 14734538]
26. Coppola T, Magnin-Luthi S, Perret-Menoud V, Gattesco S, Schiavo G, Regazzi R. Direct interaction of the Rab3 effector RIM with Ca<sup>2+</sup> channels, SNAP-25, and synaptotagmin. *J Biol Chem* 2001;276:32756–32762. [PubMed: 11438518]

27. Dai H, Tomchick DR, Garcia J, Sudhof TC, Machius M, Rizo J. Crystal Structure of the RIM2 C(2) A-Domain at 1.4 Å Resolution(.). *Biochemistry* 2005;44:13533–13542. [PubMed: 16216076]
28. Shen N, Guryev O, Rizo J. Intramolecular occlusion of the diacylglycerol-binding site in the C1 domain of munc13-1. *Biochemistry* 2005;44:1089–1096. [PubMed: 15667202]
29. Lu J, Li H, Wang Y, Sudhof TC, Rizo J. Solution structure of the RIM1α PDZ domain in complex with an ELKS1b C-terminal peptide. *J Mol Biol* 2005;352:455–466. [PubMed: 16095618]
30. Rizo J, Sudhof TC. C2-domains, structure and function of a universal Ca<sup>2+</sup>-binding domain. *J Biol Chem* 1998;273:15879–15882. [PubMed: 9632630]
31. Shao X, Davletov BA, Sutton RB, Sudhof TC, Rizo J. Bipartite Ca<sup>2+</sup>-binding motif in C2 domains of synaptotagmin and protein kinase C. *Science* 1996;273:248–251. [PubMed: 8662510]
32. Ubach J, Zhang X, Shao X, Sudhof TC, Rizo J. Ca<sup>2+</sup> binding to synaptotagmin: how many Ca<sup>2+</sup> ions bind to the tip of a C2-domain? *EMBO J* 1998;17:3921–3930. [PubMed: 9670009]
33. Fernandez I, Arac D, Ubach J, Gerber SH, Shin O, Gao Y, Anderson RG, Sudhof TC, Rizo J. Three-dimensional structure of the synaptotagmin 1 c(2)b-domain. Synaptotagmin 1 as a phospholipid binding machine. *Neuron* 2001;32:1057–1069. [PubMed: 11754837]
34. Hakes DJ, Dixon JE. New Vectors for High-Level Expression of Recombinant Proteins in Bacteria. *Analytical Biochemistry* 1992;202:293–298. [PubMed: 1519755]
35. Arac D, Chen X, Khant HA, Ubach J, Ludtke SJ, Kikkawa M, Johnson AE, Chiu W, Sudhof TC, Rizo J. Close membrane-membrane proximity induced by Ca(2+)-dependent multivalent binding of synaptotagmin-1 to phospholipids. *Nat Struct Mol Biol* 2006;13:209–217. [PubMed: 16491093]
36. Delaglio F, Grzesiek S, Vuister GW, Zhu G, Pfeifer J, Bax A. Nmrpipe - A Multidimensional Spectral Processing System Based on Unix Pipes. *Journal of Biomolecular Nmr* 1995;6:277–293. [PubMed: 8520220]
37. Johnson BA, Blevins RA. Nmr View - A Computer-Program for the Visualization and Analysis of Nmr Data. *Journal of Biomolecular Nmr* 1994;4:603–614.
38. Otwinowski Z, Minor W. Processing of X-ray diffraction data collected in oscillation mode. *Macromolecular Crystallography, Pt A* 1997;276:307–326.
39. Schneider TR, Sheldrick GM. Substructure solution with SHELXD. *Acta Crystallogr D Biol Crystallogr* 2002;58:1772–9. [PubMed: 12351820]
40. Otwinowski, Z. Isomorphous Replacement and Anomalous Scattering. Wolf, W.; Evans, PR.; Leslie, AGW., editors. Science & Engineering Research Council; Cambridge: 1991. p. 80-86.
41. Cowtan K, Main P. Miscellaneous algorithms for density modification. *Acta Crystallogr D* 1998;54:487–493. [PubMed: 9761844]
42. Murshudov GN, Vagin AA, Dodson EJ. Refinement of macromolecular structures by the maximum-likelihood method. *Acta Crystallographica Section D-Biological Crystallography* 1997;53:240–255.
43. Bailey S. The Ccp4 Suite - Programs for Protein Crystallography. *Acta Crystallographica Section D-Biological Crystallography* 1994;50:760–763.
44. Jones TA, Zou JY, Cowan SW, Kjeldgaard M. Improved Methods for Building Protein Models in Electron-Density Maps and the Location of Errors in These Models. *Acta Crystallographica Section A* 1991;47:110–119.
45. Emsley P, Cowtan K. Coot: model-building tools for molecular graphics. *Acta Crystallogr D Biol Crystallogr* 2004;60:2126–2132. [PubMed: 15572765]
46. Chen X, Tomchick DR, Kovrigin E, Arac D, Machius M, Sudhof TC, Rizo J. Three-dimensional structure of the complexin/SNARE complex. *Neuron* 2002;33:397–409. [PubMed: 11832227]
47. Dai H, Shin OH, Machius M, Tomchick DR, Sudhof TC, Rizo J. Structural basis for the evolutionary inactivation of Ca<sup>2+</sup> binding to synaptotagmin 4. *Nat Struct Mol Biol* 2004;11:844–849. [PubMed: 15311271]
48. Arac D, Murphy T, Rizo J. Facile detection of protein-protein interactions by one-dimensional NMR spectroscopy. *Biochemistry* 2003;42:2774–2780. [PubMed: 12627942]
49. Fernandez-Chacon R, Konigstorfer A, Gerber SH, Garcia J, Matos MF, Stevens CF, Brose N, Rizo J, Rosenmund C, Sudhof TC. Synaptotagmin I functions as a calcium regulator of release probability. *Nature* 2001;410:41–49. [PubMed: 11242035]

50. Rhee JS, Li LY, Shin OH, Rah JC, Rizo J, Sudhof TC, Rosenmund C. Augmenting neurotransmitter release by enhancing the apparent  $\text{Ca}^{2+}$  affinity of synaptotagmin 1. *Proc Natl Acad Sci U S A* 2005;102:18664–18669. [PubMed: 16352718]
51. Holm L, Sander C. Protein structure comparison by alignment of distance matrices. *J Mol Biol* 1993;233:123–138. [PubMed: 8377180]
52. Garcia J, Gerber SH, Sugita S, Sudhof TC, Rizo J. A conformational switch in the Piccolo C2A domain regulated by alternative splicing. *Nat Struct Mol Biol* 2004;11:45–53. [PubMed: 14718922]



**Figure 1.**

Definition of the RIM1 $\alpha$  C<sub>2</sub>B domain boundaries. (A) Domain diagrams of the different RIM proteins identified in mammals. (B) Summary of the RIM1 $\alpha$  fragments prepared to identify the boundaries of the RIM1 $\alpha$  C<sub>2</sub>B domain. On the left, bar diagrams illustrate the lengths of the different fragments, and the residue numbers of their N- and C-termini are indicated. Residues 1381 and 1615 correspond to the boundary of a splice site [splice site C; see (10)] and to the C-terminus of RIM1 $\alpha$ , respectively. The name assigned to the fragments, as well as their expression level, solubility and feasibility of purification, are qualitatively indicated on the right (N/A = not attempted).

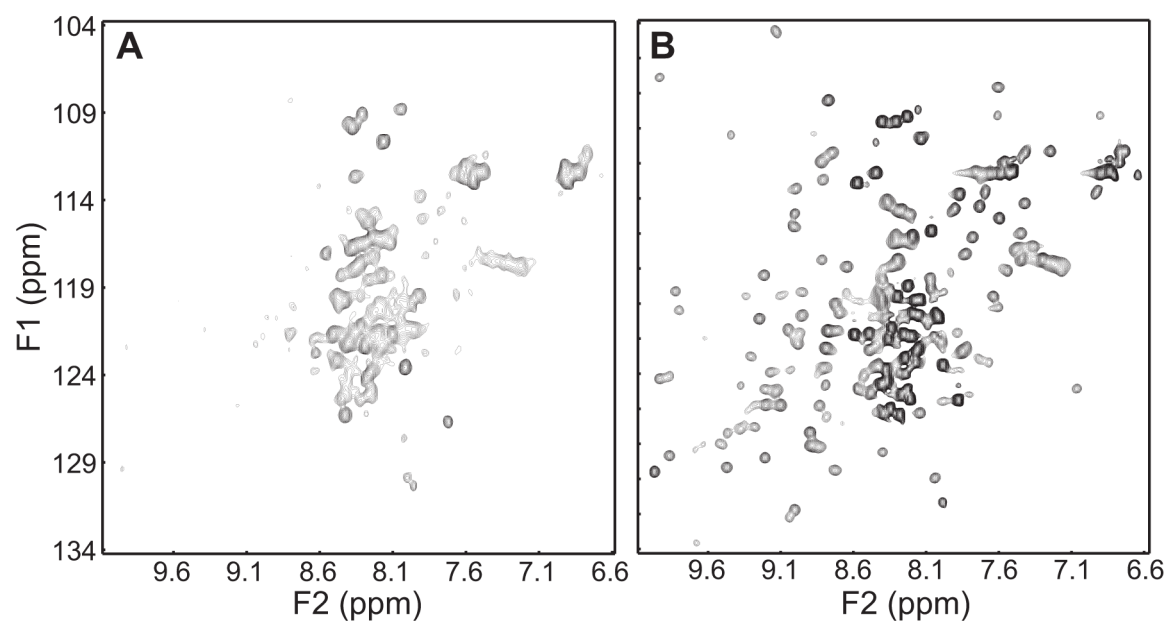


**Figure 2.**  $^1\text{H}$ - $^{15}\text{N}$  HSQC spectra of the RIM1 $\alpha$  C2B-1 (A) and C2B-3 (B) fragments acquired at 600 MHz.

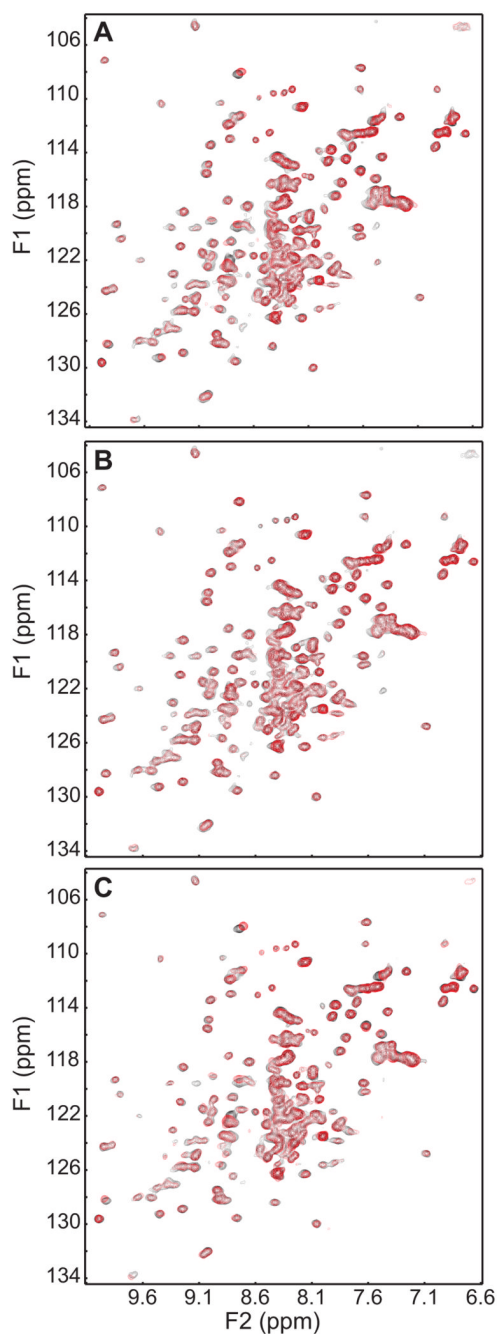


**Figure 3.**

The RIM1 $\alpha$  C<sub>2</sub>B domain does not bind to Ca<sup>2+</sup> or to the synaptotagmin 1 C<sub>2</sub> domains.

(A) <sup>1</sup>H-<sup>15</sup>N HSQC spectra of the RIM1 $\alpha$  C<sub>2</sub>B domain in the absence (black contours) and presence (red contours) of 10 mM Ca<sup>2+</sup>. (B,C) <sup>1</sup>H-<sup>15</sup>N HSQC spectra of 80  $\mu$ M <sup>15</sup>N-labeled RIM1 $\alpha$  C<sub>2</sub>B domain before (black contours) and after (red contours) addition of 100  $\mu$ M unlabeled synaptotagmin 1 C<sub>2</sub>AB fragment in the absence (B) or presence (C) of 10 mM Ca<sup>2+</sup>. All spectra were acquired at 500 MHz.

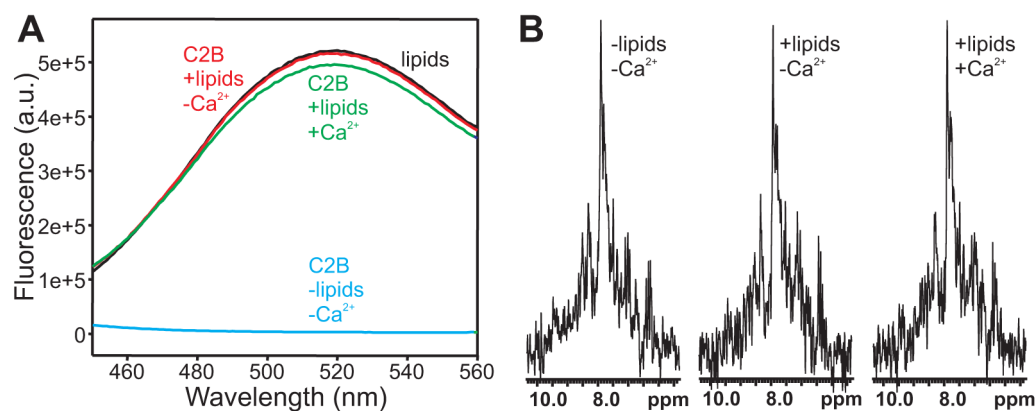


**Figure 4.**

The RIM1 $\alpha$  C<sub>2</sub>B domain does not bind to phospholipids. (A) Fluorescence spectra (excitation at 285 nm) of samples containing 0.01 mg/ml phospholipid vesicles composed of 65% PC, 25% PS and 10% dansyl-PE (black line), 1  $\mu$ M RIM1 $\alpha$  C<sub>2</sub>B domain (blue line), or 0.01 mg/ml phospholipid vesicles and 1  $\mu$ M RIM1 $\alpha$  C<sub>2</sub>B domain in 1 mM EDTA (red line) or 1 mM Ca<sup>2+</sup> (green line). (B) 1D <sup>15</sup>N-edited <sup>1</sup>H NMR spectra of 5  $\mu$ M RIM1 $\alpha$  C<sub>2</sub>B domain without (left panel) or with addition of 1 mg/ml phospholipid vesicles in the presence of 1 mM EDTA (middle panel) or 1 mM Ca<sup>2+</sup> (right panel).

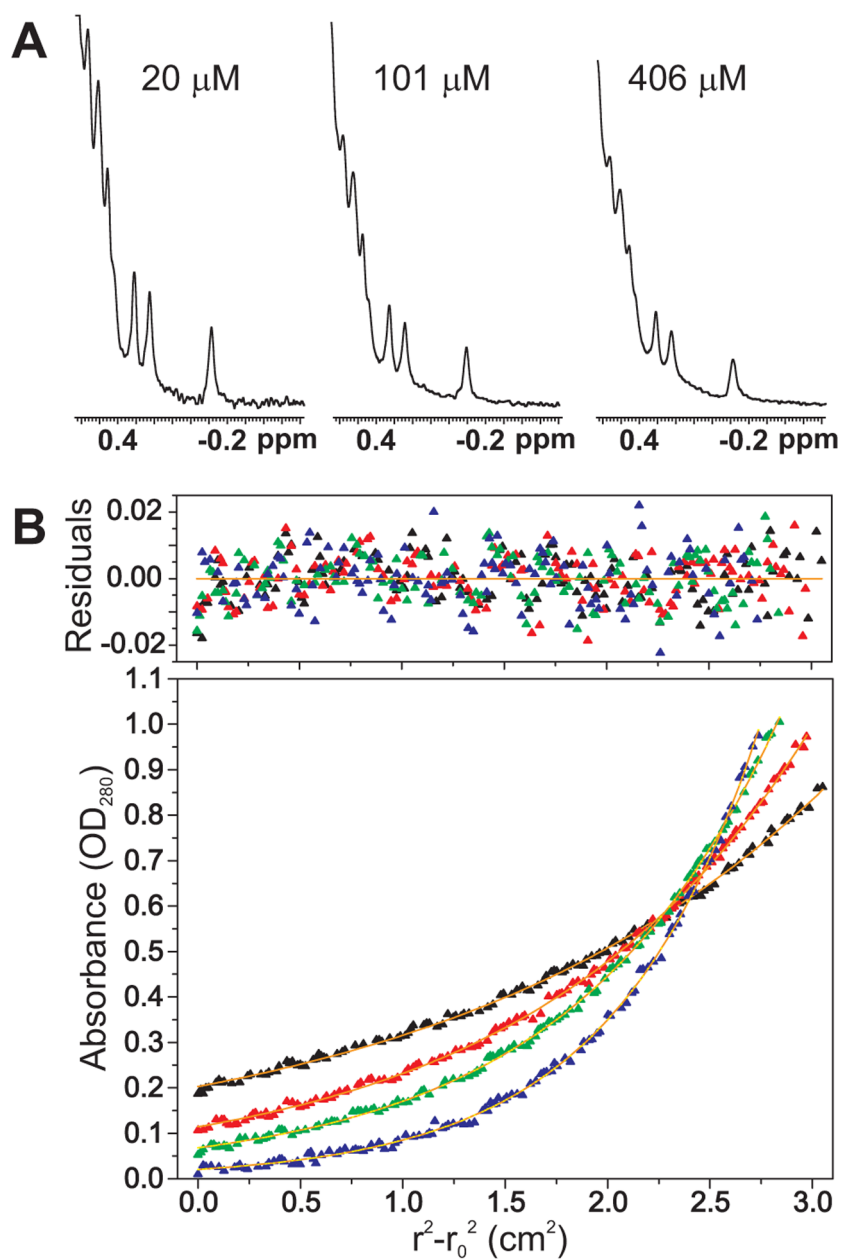


**Figure 5.**

Dimerization of the RIM1 $\alpha$  C<sub>2</sub>B domain. (A) Expansion of part of the methyl region of  $^1\text{H}$  NMR spectra of the RIM1 $\alpha$  C<sub>2</sub>B domain at 20  $\mu\text{M}$ , 101  $\mu\text{M}$  and 406  $\mu\text{M}$  concentrations. For comparison purposes, the vertical scale of the spectra was set to values that were inversely proportional to the protein concentration. (B) Equilibrium sedimentation analysis of the RIM1 $\alpha$  C<sub>2</sub>B domain. The data were obtained at centrifugation speeds of 20,000 rpm (black), 25,000 rpm (red), 29,000 rpm (green), and 35,000 rpm (blue). Curves in the bottom panel were generated by fitting the data to a monomer-dimer equilibrium model. The top panel shows the residuals.



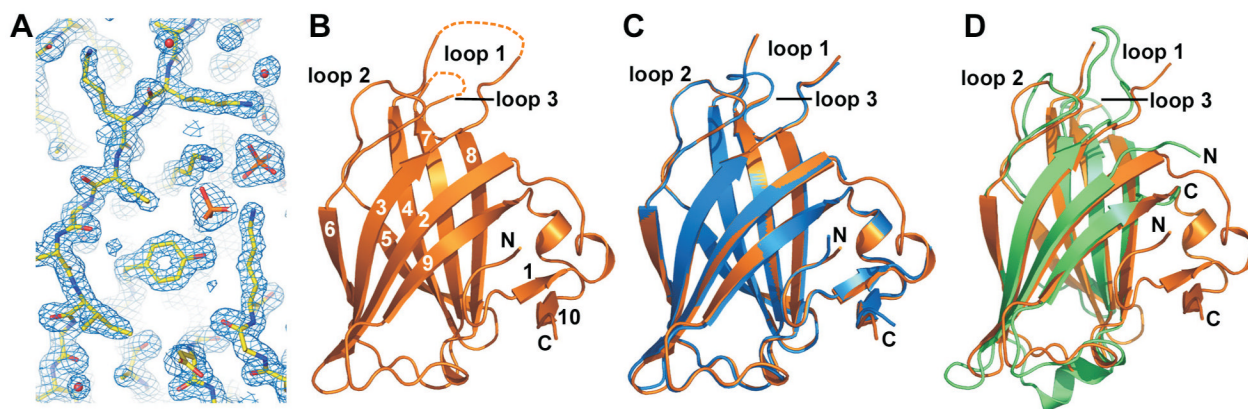


**Figure 6.**

Crystal structure of the RIM1α C<sub>2</sub>B domain. (A) A region of the 2F<sub>0</sub>–F<sub>c</sub> electron density contoured at the 1σ level. Two sulfate ions are clearly visible as tetragonal molecules with a sulfur atom in the center (orange) surrounded by four oxygen atoms (red). (B) Ribbon diagram of one of the monomers of the RIM1α C<sub>2</sub>B domain. The β-strands are labeled with numbers, and the N- and C-termini are indicated with N and C, respectively. The top loops (loops 1–3) that are commonly involved in Ca<sup>2+</sup> binding to C<sub>2</sub> domains (30) are also labeled. Note that dashed lines were used to represent arbitrary backbone conformations for a few residues in these loop that were not observable, likely due to flexibility. (C) Superposition of the two monomers found within the RIM1α C<sub>2</sub>B domain dimer. (D) Superposition of the RIM1α C<sub>2</sub>B domain (orange) with the synaptotagmin 1 C<sub>2</sub>A domain (green; PDB accession code 1RSY).

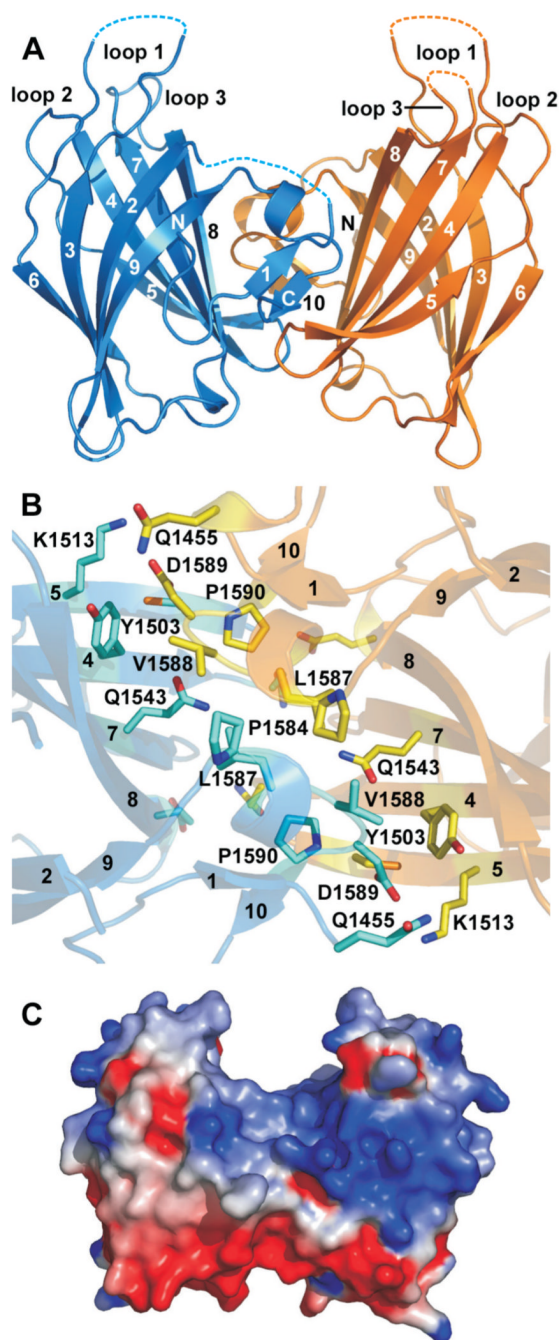


**Figure 7.**

The RIM1α C<sub>2</sub>B domain dimer. (A) Ribbon diagram of the RIM1α C<sub>2</sub>B domain dimer with one monomer colored in blue and the other in orange. The labeling scheme for β-strands, termini and top loops is the same as in Figure 6B. (B) Close-up view of the dimerization interface. The side chains from residues involved in intermolecular contacts and the Cα carbons of the same residues are shown as stick models. Oxygen atoms are in red and nitrogen atoms in blue. Carbon atoms are colored in cyan for one monomer and in yellow for the other monomer. The β-strands are labeled with the corresponding numbers, and the side chains are labeled with the one-letter amino acid code and the residue number. (C) Surface electrostatic

potential of the RIM1 $\alpha$  C<sub>2</sub>B domain dimer. The electrostatic potential was contoured at the 5 kT/e level, with red denoting negative potential and blue denoting positive potential.

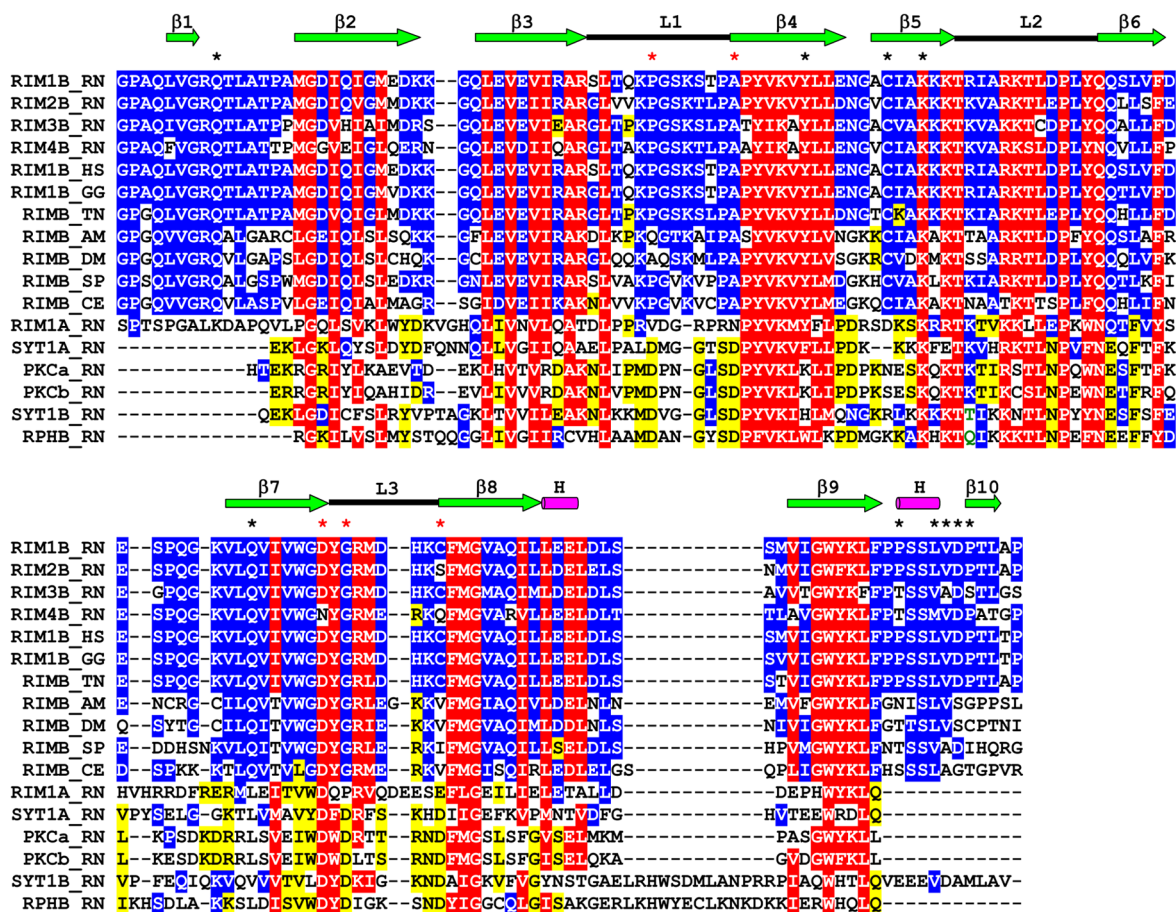


**Figure 8.**

Sequence alignment of RIM C<sub>2</sub>B domains from different species and selected rat C<sub>2</sub>-domains. Residues conserved in most C<sub>2</sub>-domains (>80% of the sequences displayed; E = D, K = R, N = Q, L = V = I = M, F = Y = W, and S = T) are colored in white with a red background. Residues that appear to be selectively conserved in RIM C<sub>2</sub>B domains are colored white with a blue background. Residues that appear to be selectively conserved in other C<sub>2</sub> domains, but not in RIM C<sub>2</sub>B domains, are colored black with a yellow background. The secondary structure elements of the rat RIM1 $\alpha$  C<sub>2</sub>B domain are shown at the top of the alignment. Helices,  $\beta$ -strands and the three top loops that are usually involved in binding of Ca<sup>2+</sup> to C<sub>2</sub> domains are represented by magenta cylinders, green arrows and black bars, respectively. The black asterisks indicate residues involved in dimerization and the red asterisks denote the positions of the five aspartate residues that are commonly involved in binding of Ca<sup>2+</sup> to C<sub>2</sub> domains (30). Protein kinase C, synaptotagmin, and rabphilin are abbreviated PKC, SYT, and RPH, respectively. A and B at the end of the protein name refers to the C<sub>2</sub>A domain and the C<sub>2</sub>B domain, respectively, whereas a and b at the end of the protein name refer to different PKC isoforms. Species abbreviations: RN, rat (*Rattus norvegicus*); HS, human (*Homo sapiens*); GG, chicken (*Gallus gallus*); TN, spotted green puffer fish (*Tetraodon nigroviridis*); DM, fruit fly (*Drosophila melanogaster*); AM, honey bee (*Apis mellifera*); SP, sea urchin (*Strongylocentrotus purpuratus*); and CE, round worm (*Caenorhabditis elegans*). GenBank entries Q9JIR4 for RIM1B\_RN, Q9JIS1 for RIM2B\_RN, Q9JIR3 for RIM3B\_RN, AAN59931.1 for RIM4B\_RN, Q86UR5 for RIM1B\_HS, XP\_419884.2 for RIM1B\_GG, CAG00377.1 for RIMB\_TN, XP\_393489.3 for RIMB\_AM, NP\_001014630.1 for RIMB\_DM, XP\_794399.2 for RIMB\_SP, Q22366 for RIMB\_CE, Q9JIR4 for RIM1A\_RN, P21707 for

SYT1A\_RN, XP\_343976 for PKCa\_RN, NP\_036845 for PKCb\_RN, P21707 for SYT1B\_RN, and NP\_598202 for RPHB\_RN.



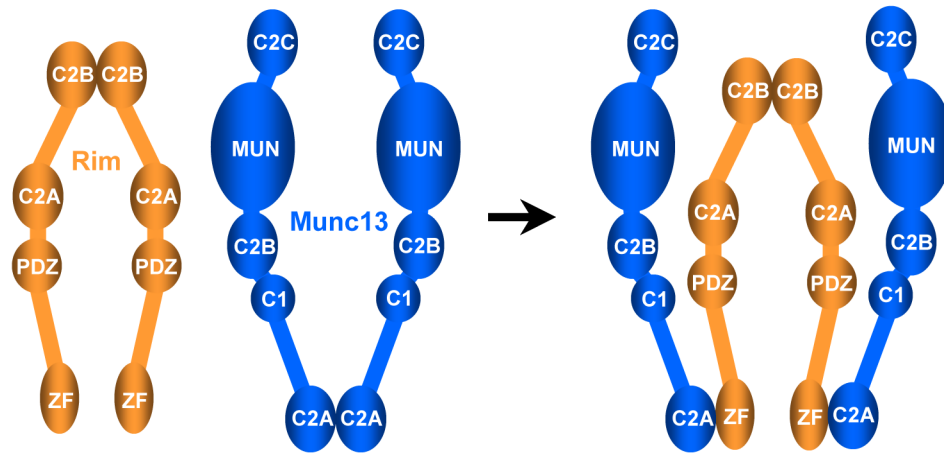


**Figure 9.**

Speculative model of how RIM1 $\alpha$  C<sub>2</sub>B domain dimerization could facilitate the Munc13-1 homodimer to Munc13-1/ $\alpha$ -RIM heterodimer switch during synaptic vesicle priming. The key aspect of the model is that the spatial proximity induced by RIM1 $\alpha$  dimerization would facilitate binding of two RIM1 $\alpha$  molecules to the two molecules that form the Munc13-1 homodimer. In contrast, binding of only one RIM1 $\alpha$  molecule would leave one of the two Munc13-1 monomers free.

**Table 1**Data collection and refinement statistics<sup>§</sup>

<b>A. Data collection</b>	
Space group	P3 <sub>1</sub> 21
Unit cell dimensions	
a, b, c (Å)	62.0, 62.0, 145.2
Wavelength (Å)	0.97918
Resolution range (Å) <sup>a</sup>	26.41-1.73 (1.76–1.73)
Data completeness <sup>a</sup>	99.9 (100.0)
R <sub>merge</sub> (%) <sup>a</sup>	5.7 (74.7)
I/β(I) <sup>a</sup>	30.9 (2.1)
Multiplicity <sup>a</sup>	7.0 (7.1)
Wilson B factor (Å <sup>2</sup> )	25.13
B. Phasing	
Anomalous scatterer	selenium (9 out of 10 possible sites)
Figure of merit (resolution range = 50.0-1.73 Å) <sup>*</sup>	0.348
C. Refinement	
Resolution range (Å) <sup>a</sup>	26.40 – 1.73 (1.78-1.73)
No. of reflections R <sub>work</sub> /R <sub>free</sub>	33,139/1,400
R <sub>work</sub> /R <sub>free</sub> (%) <sup>a</sup>	17.9 (23.2)/21.5 (28.1)
Atoms (non-H protein/water/sulfate ion/sodium ion/chloride ion)	2,256/189/35/1/3
Average B factor (Å <sup>2</sup> )	26.0
R.m.s.d. bond lengths (Å)	0.017
R.m.s.d. bond angles (°)	1.81
Missing residues	A: 1,456–1,460; 1,491–1,493 B: 1,491–1,493; 1,551–1,553
Ramachandran analysis (most favorable/allowed) (%)	88.0/12.0

<sup>§</sup>Data collection values are as defined in the program HKL2000.<sup>\*</sup> Calculated after phase refinement in the program *MLPHARE* (40).<sup>a</sup>Values in parentheses are for the highest resolution shell.
$$R_{\text{merge}} = 100 \sum_h \sum_i |I_{h,i} - \langle I_h \rangle| / \sum_h \sum_i I_{h,i}$$

where the outer sum (h) is over the unique reflections and the inner sum (i) is over the set of independent observations of each unique reflection.